3D reconstruction of magnetization from dichroic soft X-ray transmission tomography

Authors

Aurelio Hierro-Rodriguez[a1], Doga Gürsoy[bc], Charudatta Phatak[d], Carlos Quiros[ef], Andrea Sorrentino[a], Luis Manuel Alvarez-Prado[ef], Maria Velez[ef], Jose Ignacio Martin[ef], Jose Maria Alameda[ef], Eva Pereiro[a] and Salvador Ferrer[a]*

[a] ALBA Synchrotron, Carrer de la Llum, 2 - 26, Cerdanyola del Vallès, 08290, Spain

[b]Advanced Photon Source, Argonne National Laboratory, Argonne, IL, 60439, USA

[c]Department of Electrical Engineering and Computer Science, Northwestern University, Evanston, IL, 60208, USA

[d]Materials Science Division, Argonne National Laboratory, Argonne, IL, 60439, USA

[e]Departamento de Física, Universidad de Oviedo, Oviedo, 33007, Spain

[f]Centro de Investigación en Nanomateriales y Nanotecnología, CINN (CSIC - Universidad de Oviedo), El Entrego, 33940, Spain

Correspondence email: ferrer@cells.es

[1]Present Address: SUPA, University of Glasgow, School of Physics and Astronomy, G12 8QQ, Glasgow, UK.

Funding information Spanish MINECO (grant No. FIS2013-45469; grant No. FIS2016-76058 (AEI/FEDER, EU); contract No. FIS2016-76058 (AEI/FEDER, EU) to Aurelio Hierro-Rodriguez); FICYT-Asturias (grant No. FC-GRUPIN14-040); U.S. Department of Energy (DOE) Office of Science User Facility operated for the DOE Office of Science by Argonne National Laboratory (contract No. DE-AC02-06CH11357 to Doga Gürsoy); U.S. Department of Energy, Office of Science, Office of Basic Energy Sciences, Material Sciences and Engineering Division (contract to Charudatta Phatak).

Synopsis By using Soft X-ray transmission microscopy with magnetic contrast (magnetic circular dichroism) it is possible to get valuable magnetic information from the studied systems. In this work we go a step further presenting a method to use Magnetic Soft X-ray transmission tomography as an ideal tool to reconstruct the 3D magnetization configuration of arbitrary magnetic samples.

Abstract The development of magnetic nanostructures for applications in spintronics requires methods capable of visualizing their magnetization. Soft X-ray magnetic imaging combined with circular magnetic dichroism allows to probe nanostructures up to 100-300 nm in thickness with resolutions of 20-40 nm. Here we present a new iterative tomographic reconstruction method to extract the three-dimensional (3D) magnetization configuration from tomographic projections. The vector field is reconstructed by using a modified algebraic reconstruction approach based on solving a set of linear equations in an iterative manner. The application of this method is illustrated with two examples (magnetic nano-disc and micro-square heterostructure) along with comparison of error in reconstructions, and convergence of the algorithm.

Keywords: Soft X-ray Transmission Microscopy; X-Ray Transmission Tomography; Vector Field Tomography; Magnetization Configuration Reconstruction

1. Introduction

Advances in nanomagnetism towards applications in spintronics involve magnetic heterogeneous systems with increasing complexity including multiple materials, and complex geometries. Spectroscopic methods and imaging tools are required to characterize and visualize the local magnetic properties at different regions throughout the heterostructures. Several tools for magnetic imaging have been developed in the past years. Using visible light photons, Kerr microscopy and Vector Magnetometry provide, via magneto-optical effects, mappings of the magnetization with lateral resolutions around ~1 μm limited by the photon wavelengths [1-3]. Their probing depth is of few nm in metallic samples. Higher lateral resolution is achieved with electron-based techniques by using secondary or photo emitted electrons. Scanning electron microscopy with polarization analysis and X-ray photoemission electron microscopy provide very good lateral resolution (~10 nm) but they also have shallow probing depths (1-2 nm) due to strong inelastic scattering of low energy electrons [4-7]. This limitation is circumvented for high energy electrons that traverse samples. Lorentz Transmission Electron Microscopy (Lorentz TEM) [8, 9] has an excellent lateral resolution (~1 nm) and is sensitive to the magnetization of the whole sample in systems up to ~100 nm thickness. Because the technique probes the magnetization perpendicular to the direction of the propagation of electrons, it is highly sensitive to in-plane magnetization. A further development of Lorentz TEM, which is called the Vector Field Electron Tomography, is especially interesting [10, 11]. It combines both, the excellent lateral resolution and the in-depth magnetic sensitivity of Lorentz TEM, with the 3D volume reconstruction capabilities of tomography to obtain the potential vector **A** and from it, the full magnetization configuration in 3D magnetic systems. Besides these methods, two X-ray based techniques are being used to probe magnetization with high sensitivity and spatial resolution. Soft X-ray transmission microscopy using circularly polarized X-rays of energies typically below 1 keV with a 100-300 nm penetration depth, has been used to image buried magnetic layers by exploiting the large magnetic dichroism occurring at specific electronic transitions in magnetic atoms [12, 13]. More

recently, hard X-rays (photon energies of about 6-10 keV) that have larger penetration depths (~μm), have been successfully used to reconstruct 3D magnetization. In this case, as the magnetic dichroic absorption is very small compared to soft X-rays, the method uses transversally coherent X-rays to exploit diffraction and phase contrast in ptychography mode, which involves the acquisition of several thousands (~10^5) of diffraction images, allowing to resolve the magnetization of the sample with lateral resolution around 100 nm typically [14].

Here we present the development of a new iterative algorithm to obtain quantitative 3D vector magnetization reconstruction using soft X-ray microscopy [12, 15, 16]. This is achieved by taking X-ray transmission images with opposite dichroism (positive and negative), for two tomogram series by rotating the object around two orthogonal tilt axes. The total number of images required is around 500 or less. The reconstructions are based on a joint processing of both tomogram series for obtaining the reconstructed magnetic configuration. Section 2 presents the forward problem of magnetic soft X-ray transmission microscopy by introducing the equations that describe the projected images. In section 3, we analyze scalar and vector field reconstruction problems solving them by using a modified iterative algebraic reconstruction technique. The algorithm will be made openly available under TomoPy, which is a library for tomographic image reconstruction [17] and the simulated tomograms will be accessible through TomoBank [18]. Section 4 illustrates the application of the method by reconstructing two simulated magnetic microstructures and evaluating its accuracy. Finally, the conclusions of the work are presented in section 5.

2. Magnetic Soft X-ray Transmission Microscopy

In an X-ray transmission microscope, the transmitted X-ray intensity through the sample under investigation is recorded at each pixel of a 2D detector forming a transmission image. In what follows, we assume a simplified geometry with incoming parallel beam, although the condenser optics of the Soft X-ray microscope focuses the beam onto the sample, and the objective Fresnel Zone plate lens (FZP) collects the transmitted beam producing a magnified image (x1500) at the charged-coupled detector (CCD) [19]. The FZP has a limited depth of field that will affect the projections while rotating, if the sample size exceeds it. This has to be taken into account for samples with relatively large lateral dimensions. Exploiting the broad photon energy spectrum emitted by synchrotron light-sources, it is possible to tune the X-ray wavelength in order to match atom-specific absorption edges leading also to resonant atom-specific images [19, 20]. Moreover, if the polarization of the incident beam is circular (right or left handed), atom-specific magnetic images can be recorded by taking advantage of Magnetic Dichroism effect [20, 21]. In this framework, the X-ray intensity after passing through the sample can be described as follows:

$$I = I_0 \exp\left(\int L^{-1}\left[1 + \delta\left(\vec{k} \bullet \vec{m} \right) \right] dt \right) \quad (1)$$

In equation 1, I and I_0 are the transmitted and incident intensities of the X-ray beam respectively; L^{-1} is the inverse of the attenuation length for the X-rays. It depends on the photon energy and on electron density of the sample which will be variable in heterogeneous systems; δ is the dichroic coefficient for the magnetic material under analysis. It is the scale factor of the magnetic sensitivity and depends on the electronic levels of the absorbing atoms; $\boldsymbol{k}\bullet\boldsymbol{m}$ is the dot product of X-ray wave vector and magnetization. It provides the sensitivity of the dichroism at different relative orientations of the sample and the photon beam; **m** is the reduced magnetization vector ($\boldsymbol{m} = \boldsymbol{M}/M_S$, with $\boldsymbol{M}$ the magnetization vector and M_S the saturation magnetization); and dt is the elementary path along the X-ray linear trajectory spanned by the line integral. The latter runs along the entire beam path, from its source to the detector, passing through the sample space. Thus, it is clear that, L^{-1}, δ and $\boldsymbol{m}$ are implicit functions of t as they are sampled by the X-ray beam. The transmittance ($T = I/I_0$) is separated in two terms:

$$T = \exp\left(\int L(t)^{-1} dt + \int L(t)^{-1} \delta(t) \left[\vec{k} \bullet \vec{m}(t) \right] dt \right) \quad (2)$$

The first integral does not depend on the magnetism but only on the charge distribution in the sample whereas the second one includes the magnetic contributions. For practical convenience and to separate the magnetic and nonmagnetic parts we take the logarithms of the transmittance for right handed ($+\delta$, Eq. 3a) and left handed polarizations ($-\delta$, Eq. 3b).

$$\log\left[T_{+\delta}\right] = \int L(t)^{-1} dt + \int L(t)^{-1} \delta(t) \left[\vec{k} \bullet \vec{m}(t) \right] dt \quad (3a)$$

$$\log\left[T_{-\delta}\right] = \int L(t)^{-1} dt - \int L(t)^{-1} \delta(t) \left[\vec{k} \bullet \vec{m}(t) \right] dt \quad (3b)$$

Hence, by simply adding and subtracting equations 3a and 3b, separate expressions for the non-magnetic (Eq. 4a) and magnetic (Eq. 4b) contributions are obtained.

$$\log\left[T_{+\delta}\right] + \log\left[T_{-\delta}\right] = 2\int L(t)^{-1} dt \quad (4a)$$

$$\log\left[T_{+\delta}\right] - \log\left[T_{-\delta}\right] = 2\int L(t)^{-1} \delta(t) \left[\vec{k} \bullet \vec{m}(t) \right] dt \quad (4b)$$

Equation 4a will be used to obtain the values of the attenuation length (L), which is a scalar field while equation 4b will allow extracting the magnetization configuration ($\boldsymbol{m}$) of the system.

3. Scalar and Vector Field Tomographic Reconstruction

In a general tomography problem, a certain property of an unknown sample is volume reconstructed by the analysis of its different projections [22]. These are acquired by taking images of the sample at different rotation angles around a certain axis or axes.

Figure 1a shows a picture of the general problem for transmitted X-rays (red arrows) and two orthogonal rotation axes. We indicate as *Xtilt* and *Ytilt* the projection series acquired by rotating the system around X and Y axes respectively. The sample is located between the X-ray source and the detector. Both rotation axes pass through the centre of the sample taken as the origin of the reference frame. In the sample space, a volume model formed by voxels is created (grey cube around the sample in Fig. 1a) with its centre located at the origin.

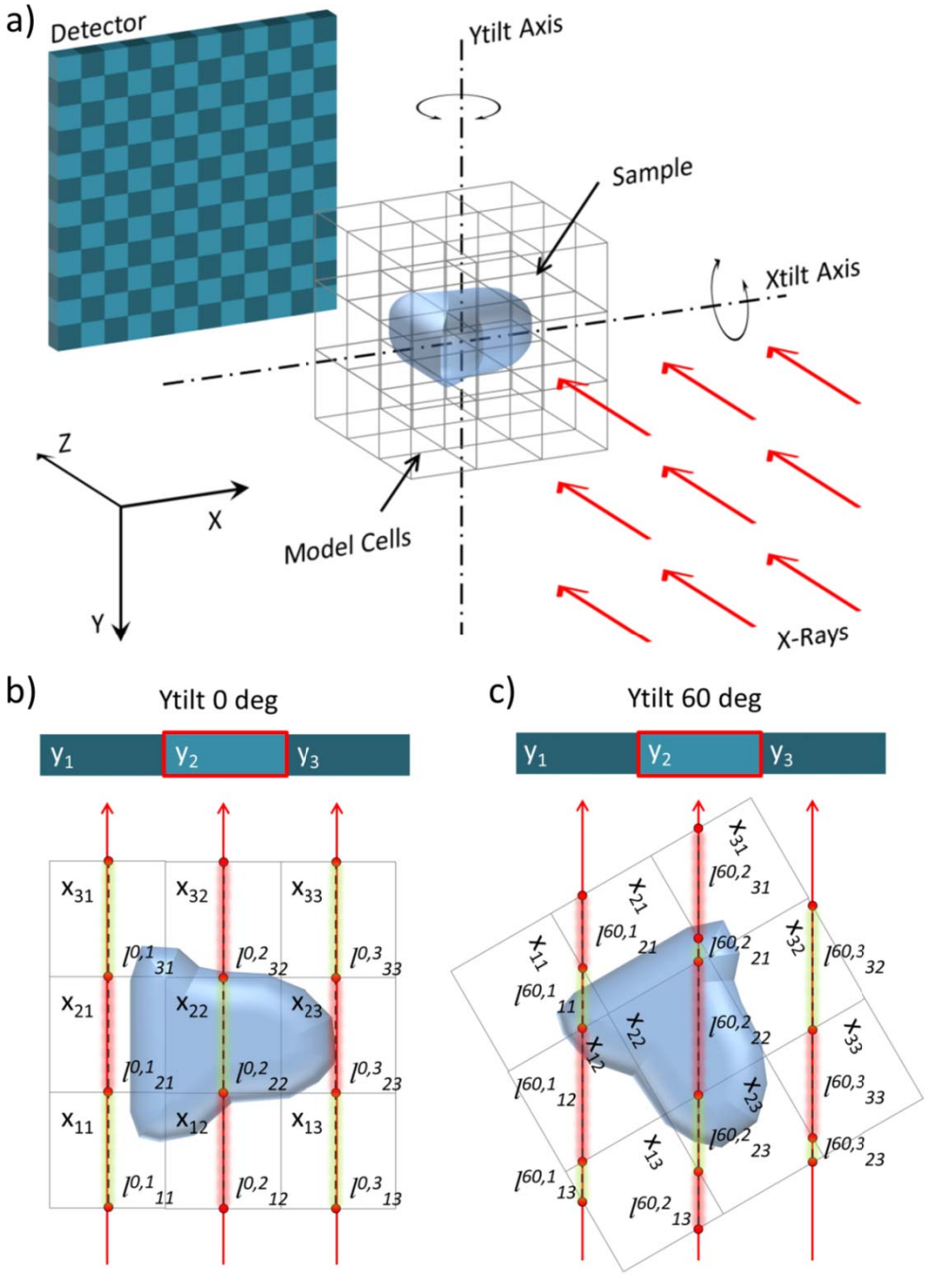

Figure 1 (a) Scheme of the tomography problem showing the X-ray beam, the sample, the rotation axes, the detector and a volume model for the reconstruction. Two projections at 0 (b) and 60 (c) degrees rotated around the Y axis (plane XZ) on a 1D detector are also presented.

Let's call "x" the property that we want to reconstruct, thus each voxel of the model will contain a value for this parameter. In order to get the x field by using the volume model, the images recorded with the detector at different projection angles (measured data) are compared with the mathematic projection of the model at the same tilt angles. In this way, the problem to reconstruct the x field can be written as a system of linear equations in the following form:

$$y^{\phi} - A^{\phi}x = 0 \quad (5)$$

$$y^{\phi} = \begin{bmatrix} y^{\phi}_{1,1} \\ \vdots \\ y^{\phi}_{n,m} \\ \vdots \\ y^{\phi}_{N,M} \end{bmatrix} \quad , \quad x = \begin{bmatrix} x_{1,1,1} \\ \vdots \\ x_{i,j,k} \\ \vdots \\ x_{I,J,K} \end{bmatrix} \quad , \quad A^{\phi} = \begin{bmatrix} l^{\phi,1,1}_{1,1,1} & \cdots & l^{\phi,1,1}_{i,j,k} & \cdots & l^{\phi,1,1}_{I,J,K} \\ \vdots & \ddots & & & \vdots \\ l^{\phi,n,m}_{1,1,1} & & l^{\phi,n,m}_{i,j,k} & & l^{\phi,n,m}_{I,J,K} \\ \vdots & & & \ddots & \vdots \\ l^{\phi,N,M}_{1,1,1} & \cdots & l^{\phi,N,M}_{i,j,k} & \cdots & l^{\phi,N,M}_{I,J,K} \end{bmatrix}$$

The column vector $\boldsymbol{y}^{\phi}$ represents the transmittance at each pixel of the detector arranged in raster order (concatenated stacking of all the rows of the detector) for a certain projection ϕ. The detector has N x M pixels. The column vector $\boldsymbol{x}$ is composed by the values for the x field stored in the volume model arranged also in raster order [concatenated stacking of volume model data ordered by running the rows (j index), the columns (i index) and finally the layers (k index)]. The general volume model has I x J x K voxels, indicating the number of rows, columns and layers respectively. The matrix A^{ϕ} is the projection matrix which allows to obtain the values of each detector pixel $\boldsymbol{y}^{\phi}$ as a function of the model parameters $\boldsymbol{x}$ for a certain projection angle ϕ. This matrix has size (NM x IJK) and is sparse. Its elements ($l^{\phi,n,m}_{i,j,k}$) are indexed indicating to which detector pixel (n,m) and at which tilt angle (ϕ) the volume is being projected, and also what cell of the model (i,j,k) is involved. The main point here is that for different projections, different linear combinations of the voxels contribute to the integrated intensity in the same detector pixel. Thus, the value of each element of A^{ϕ} is calculated as the length of a specific ray through each voxel at a projection angle ϕ. These lengths are the "weights" of the physical property enclosed in the voxels (x) to form the linear combination determined by the beam. It is important to mention here that an efficient implementation of the calculation of these elements is crucial for the performance of the final reconstruction algorithm [23,24].

To further clarify this point, we analyse a simple example of two different projections in the *Ytilt* configuration at 0 (Fig.1b) and 60 (Fig.1c) degrees. The presented situation is reduced to a single row (1D) of the detector with 3 pixels (y_1, y_2, y_3) and a 2D slice ($x_{1,1}$, … ,$x_{i,j}$, … ,$x_{3,3}$) in the XZ plane (*Ytilt*) of the volume model. The length of the X-ray beam inside each cell ($l^{\phi,n}_{i,j}$) is indexed using the

previous convention. Thus, for instance the linear combination resulting in the signal integrated by pixel 2 for 0 and 60 degrees projection can be written as $y_2^0 = l_{1,2}^{0,2}x_{1,2} + l_{2,2}^{0,2}x_{2,2} + l_{3,2}^{0,2}x_{3,2}$, and $y_2^{60} = l_{1,3}^{60,2}x_{1,3} + l_{2,3}^{60,2}x_{2,3} + l_{2,2}^{60,2}x_{2,2} + l_{2,1}^{60,2}x_{2,1} + l_{3,1}^{60,2}x_{3,1}$.

It is clear now that the line integral appearing in equation 4a is numerically reproduced by this linear combination along the X-ray path. The L^{-1} values are considered homogeneous inside each voxel and the infinitesimal line integral element (*dt*) is substituted by the length of the ray through the involved model cell. The resulting equations system has as many equations as the number of detector pixels times the number of different projection angles. For instance, a 256 x 256 pixels detector and 100 projections leads to a system with more than 6.5 million equations. To solve this problem we use the Algebraic Reconstruction Technique (ART) [22]. First, an initial value (it can be 0) is assigned to the parameters contained in the model voxels. After this, the volume model is projected into the detector space by using A^ϕ for the initial tilt angle of the tomogram. By calculating the difference between the experimental data ($\boldsymbol{y}^\phi$) and the numerically projected one, an error vector ($\boldsymbol{e}^\phi$) is obtained as depicted in equation 6.

$$e^\phi = y^\phi - A^\phi x \quad (6)$$

The model parameters are updated as indicated in equation 7. Vectors $\boldsymbol{x}^{new}$ and $\boldsymbol{x}^{old}$ represent the model parameters after and before of update respectively. C^ϕ and R^ϕ are diagonal matrices where each one of their elements is calculated as the inverse of the sum of all column and row elements in matrix A^ϕ respectively. For their calculation, indices "*c*" and "*r*" indicate the column and row index of the projection matrix A^ϕ respectively, thus they run from 1 to *IJK* for index *c* and from 1 to *NM* for index *r*. These matrices are included in order to compensate for the number of beams interacting with the same voxel, and for the number of pixels which are hit by the same ray, thus they prevent for overweighting. Finally, $[A^\phi]^T$ represents the transposed A^ϕ matrix.

$$x^{new} = x^{old} + \left[C^\phi \left[A^\phi \right]^T R^\phi \right] e^\phi \quad (7)$$

$$C^\phi = \begin{bmatrix} c_{1,1}^\phi & 0 & \cdots & & 0 \\ 0 & \ddots & & & \\ \vdots & & c_{c,c}^\phi & & \vdots \\ & & & \ddots & 0 \\ 0 & & \cdots & 0 & c_{IJK,IJK}^\phi \end{bmatrix}, \quad c_{c,c}^\phi = \frac{1}{\sum_r l_{r,c}^\phi}$$

$$R^\phi = \begin{bmatrix} r_{1,1}^\phi & 0 & \cdots & & 0 \\ 0 & \ddots & & & \\ \vdots & & r_{r,r}^\phi & & \vdots \\ & & & \ddots & 0 \\ 0 & & \cdots & 0 & r_{NM,NM}^\phi \end{bmatrix}, \quad r_{r,r}^\phi = \frac{1}{\sum_c l_{r,c}^\phi}$$

Note here that an iteration is completed when all the recorded projections are taken into account to update the model, thus to complete an iteration by using the scheme shown in equation 7 we apply the following protocol: 1) calculate the A^{ϕ} matrix for the 1st projection angle and calculate the error vector e^{ϕ} for that angle, 2) update the model using equation 7. After this, go back to step 1) but using the 2nd projection angle instead of the first one and calculate the error using the previously updated model, update the model again with the new error and continue repeating the protocol until the last projection is taken into account. One iteration is said to be complete, when all the projection angles have been processed once. By performing several iterations the solution for the reconstructed field converges, which is common to ART. We have chosen ART for the iterative reconstruction due to the fast convergence (8 – 10 iterations usually lead to convergence) and because the method does not assumes any a priori information related with the noise or object model.

This method can be directly applied in order to reconstruct scalar fields for the situation shown in equation 4a to reconstruct the attenuation length in 3D. In order to apply the protocol to reconstruct vector field as in the case of equation 4b, it is only necessary to calculate a different projection matrix which takes into account the signal recorded with magnetic contrast due to the dot product. To do this we express the X-ray wave vector in spherical coordinates ($k_x = \sin\theta\cos\varphi$, $k_y = \sin\theta\sin\varphi$, $k_z = \cos\theta$) and perform the dot product (Eq. 8).

$$\log\left[T_{+\delta}\right] - \log\left[T_{-\delta}\right] = 2\int L(t)^{-1}\,\delta(t)\left[\sin\theta\cos\varphi\, m_x(t) + \sin\theta\sin\varphi\, m_y(t) + \cos\theta\, m_z(t)\right]dt \quad (8)$$

Note here that the previously used projection angle defined as ϕ is the same as θ in spherical coordinates. In the reference frame as sketched in figure 1, *Ytilt* series implies a rotation of an angle θ with a fixed angle $\varphi = 0$ degrees (defining the XZ plane). In the case of *Xtilt* series, the fixed φ angle is 90 degrees and the rotation angle is equally θ (defining the YZ plane). This means that with only one tilt series it is not possible to reconstruct all the components of the magnetization vector, thus to get the necessary information, we acquire two tomogram series: one around the Y axis (*Ytilt*), and other around the X axis (*Xtilt*). The first one will give information about m_x and m_z components (Eq. 9a), while the second one contains information from m_y and m_z (Eq. 9b).

$$Ytilt \longrightarrow \log\left[T_{+\delta}\right] - \log\left[T_{-\delta}\right] = 2\int L(t)^{-1}\,\delta(t)\left[\sin\theta\, m_x(t) + \cos\theta\, m_z(t)\right]dt \quad (9a)$$

$$Xtilt \longrightarrow \log\left[T_{+\delta}\right] - \log\left[T_{-\delta}\right] = 2\int L(t)^{-1}\,\delta(t)\left[\sin\theta\, m_y(t) + \cos\theta\, m_z(t)\right]dt \quad (9b)$$

The vector field reconstruction projection matrix will need to take into account now, not only the length of the ray through each voxel, but also the projection angle sine and cosine due to the magnetic contrast. As we are working now with two different tilt series; for the same projection angle θ we

have two different images acquired (one from *Ytilt* and other from *Xtilt*). We can arrange the data in the form of a column vector as in the scalar case, but now concatenating the *Xtilt* data after the *Ytilt* one. Also it is necessary to create a volume model where now, each voxel contains three parameters which are the three magnetization vector components. In this way, the linear equations system for the vector field case can be written as follows.

$$y^{\varphi,\theta} - A^{\varphi,\theta}x = 0 \quad (10)$$

$$y^{\varphi,\theta} = \begin{bmatrix} y_{1,1}^{0,\theta} \\ \vdots \\ y_{n,m}^{0,\theta} \\ \vdots \\ y_{N,M}^{0,\theta} \\ y_{1,1}^{90,\theta} \\ \vdots \\ y_{n,m}^{90,\theta} \\ \vdots \\ y_{N,M}^{90,\theta} \end{bmatrix}, \quad x = \begin{bmatrix} x_{1,1,1}^{X} \\ \vdots \\ x_{i,j,k}^{X} \\ \vdots \\ x_{I,J,K}^{X} \\ x_{1,1,1}^{Y} \\ \vdots \\ x_{i,j,k}^{Y} \\ \vdots \\ x_{I,J,K}^{Y} \\ x_{1,1,1}^{Z} \\ \vdots \\ x_{i,j,k}^{Z} \\ \vdots \\ x_{I,J,K}^{Z} \end{bmatrix}, \quad A^{\varphi,\theta} = \begin{bmatrix} \sin\theta\, B^{0,\theta} & 0 & \cos\theta\, B^{0,\theta} \\ 0 & \sin\theta\, B^{90,\theta} & \cos\theta\, B^{90,\theta} \end{bmatrix}$$

$$B^{0,\theta} = \begin{bmatrix} l_{1,1,1}^{0,\theta,1,1} & \cdots & l_{i,j,k}^{0,\theta,1,1} & \cdots & l_{I,J,K}^{0,\theta,1,1} \\ \vdots & & \vdots & & \vdots \\ l_{1,1,1}^{0,\theta,n,m} & \cdots & l_{i,j,k}^{0,\theta,n,m} & \cdots & l_{I,J,K}^{0,\theta,n,m} \\ \vdots & & \vdots & & \vdots \\ l_{1,1,1}^{0,\theta,N,M} & \cdots & l_{i,j,k}^{0,\theta,N,M} & \cdots & l_{I,J,K}^{0,\theta,N,M} \end{bmatrix}, \quad B^{90,\theta} = \begin{bmatrix} l_{1,1,1}^{90,\theta,1,1} & \cdots & l_{i,j,k}^{90,\theta,1,1} & \cdots & l_{I,J,K}^{90,\theta,1,1} \\ \vdots & & \vdots & & \vdots \\ l_{1,1,1}^{90,\theta,n,m} & \cdots & l_{i,j,k}^{90,\theta,n,m} & \cdots & l_{I,J,K}^{90,\theta,n,m} \\ \vdots & & \vdots & & \vdots \\ l_{1,1,1}^{90,\theta,N,M} & \cdots & l_{i,j,k}^{90,\theta,N,M} & \cdots & l_{I,J,K}^{90,\theta,N,M} \end{bmatrix}$$

The elements of the $\boldsymbol{y}^{\varphi,\theta}$ column vector are indexed as $y_{n,m}^{\varphi,\theta}$ where φ and θ indicate if the data is related to the *Ytilt* ($\varphi = 0$) or *Xtilt* ($\varphi = 90$) series, and the value of the projection angle respectively. The sub-indices *n* and *m* specify the pixel in the detector as in the scalar case. Now, this column vector has 2(*N* x *M*) elements. The column vector containing the volume model parameters has 3(*I* x *J* x *K*) elements and is arranged by concatenating the *X*, *Y* and *Z* components of the vector property to be reconstructed. Their elements are labelled indicating the voxel index (*i*,*j*,*k*) and the vector component (*X*,*Y* or *Z*). Due to these new sizes for detector and volume model vectors, the projection matrix $A^{\varphi,\theta}$ has 2(*NM*) x 3(*IJK*) elements, and due to the selected arrangement of $\boldsymbol{y}^{\varphi,\theta}$ and $\boldsymbol{x}$ vectors, its

arrangement is different from the scalar case. The matrix can be separated in six different blocks arranged in two rows and three columns. Each block is a sub-matrix of size *NM* x *IJK* and allows for the projection of a different vector component in the *Ytilt* or *Xtilt* situation. The first row is referred to the *Ytilt* projection and the second one to the *Xtilt.* The three columns are related with *X*, *Y* and *Z* vector field components respectively. Thus, by using equations 9a and 9b, the first row supports for the reconstruction of *X* and *Z* components of the vector field, while the second one deals with *Y* and *Z*. This means that first-row second-column and second-row first-column blocks are zeros. First-row first-column and second-row second-column blocks are multiplied by $\sin\theta$ to project m_x and m_y respectively and both row block-elements of the third-column project m_z and are multiplied by $\cos\theta$. The base sub-matrices are indicated as $B^{0,\theta}$ and $B^{90,\theta}$. They are calculated as the projection matrix in the scalar case and contain the lengths of the analysed ray passing through the model voxels in the *Ytilt* and *Xtilt* configurations respectively. The elements of matrices $B^{0,\theta}$ and $B^{90,\theta}$ are labelled as $l_{i,j,k}^{0,\theta,n,m}$ and $l_{i,j,k}^{90,\theta,n,m}$ indicating the *Ytilt* ($\varphi = 0$) or *Xtilt* ($\varphi = 90$) configuration, the detector pixel (n,m), and the voxel index in the volume model (i,j,k).

ART can be directly applied to the equation system described in Eq. 10 as it was applied for the reconstruction of a scalar field; the only difference is that matrices *C* and *R* must be calculated with $A^{\varphi,\theta}$ without multiplying its sub-matrix elements ($B^{0,\theta}$ and $B^{90,\theta}$) by $\sin\theta$ and $\cos\theta$. This is because C and R matrices only compensate for the number of beams interacting with the same voxel and for the number of pixels which are hit by the same ray. Finally, it is important to note, that we are not directly reconstructing the reduced magnetization vector; we are reconstructing $2L(t)^{-1}\delta(t)\boldsymbol{m}(t)$ (Eq. 4b). The contribution of the attenuation length can be easily accounted for by using the scalar field reconstruction using equation 4(a), and then using those values in the model to isolate $\delta(t)\boldsymbol{m}(t)$. The latter is proportional to the magnetization configuration.

4. Reconstruction of Magnetic Micro/Nanoparticles

Two different magnetic particles have been simulated in order to test the capabilities of the aforementioned reconstruction approach: a Permalloy ($Ni_{80}Fe_{20}$, Py) nano-disc and a Py/Al/Py micro-square heterostructructure (Fig. 2).

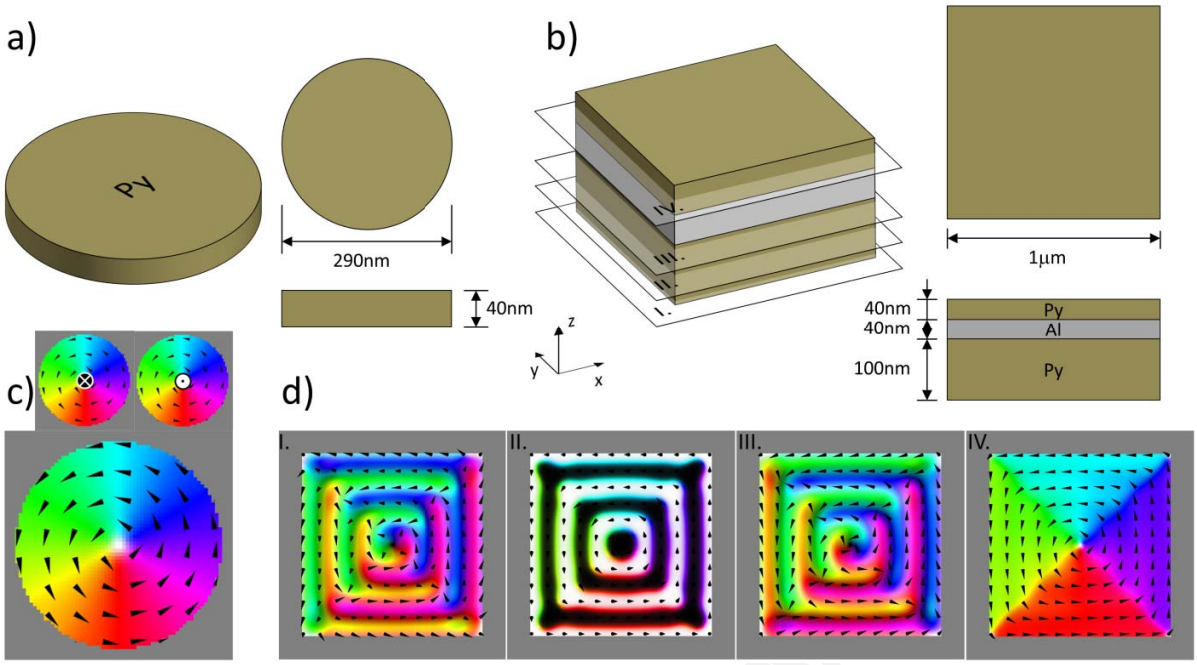

Figure 2 Schematics of the magnetic nano-disc (a) and micro-square (b) systems simulated to test the vector reconstruction algorithm. The relaxed magnetic configuration of both structures is presented showing simulation volume slices in the disc (c) and square (d) cases.

The micromagnetic simulations have been performed by using the Mumax3 code [25]. The systems have been simulated using 5 x 5 x 5 nm^3 cells with Ms of Py = $810x10^3$ A/m, exchange stiffness A_{exch} = $1.3x10^{-11}$ J/m, and an out-of-plane uniaxial anisotropy energy density K_U = $6x10^4$ J/m^3. The latter is usually present in Py structures and supports the formation of stripe domains in thicker samples, [26] but it is not generally considered in thin film simulations due to its negligible contribution in comparison with Py thin film shape anisotropy term (which is 2 orders of magnitude larger). In our case, as we are going to simulate a rather thick magnetic heterostructure, it needs to be taken into account. The Py disc was 290 nm in diameter and a thickness of 40 nm. It presents a clear vortex configuration at remanence as represented from the central slice of the simulation [Fig. 2(c)]. The colour scale for the magnetization orientation is represented by small vortices with opposite polarities (Black → m_z negative, white → m_z positive).

The micro-particle consists of a 1 µm side square with 100nm/40nm/40nm thickness structure of Py/Al/Py respectively. Different slices of the simulation showing the magnetization configurations at remanence are presented for the thick Py layer [I. – III., Fig. 2(d)] and for the thin one [IV., Fig. 2(d)]. The system supports stripe domains in the thick Py layer and mainly in-plane magnetization is present in the thin one. This decoupling is mediated by the non-magnetic Al spacer. The output of the micromagnetic simulation encloses the reduced magnetization vector at each simulation cell. This is combined with a model containing the attenuation length of each material for the Fe L3 energy edge (Py → L^{-1} = $5.13x10^6$ m^{-1}, Al → L^{-1} = $8.24x10^5$ m^{-1}), and a dichroic factor of 0.22 only where the Py is

present. By projecting these models using the equation 4b, we simulate the X-ray transmission tomography data which will be used to test the reconstruction algorithm.

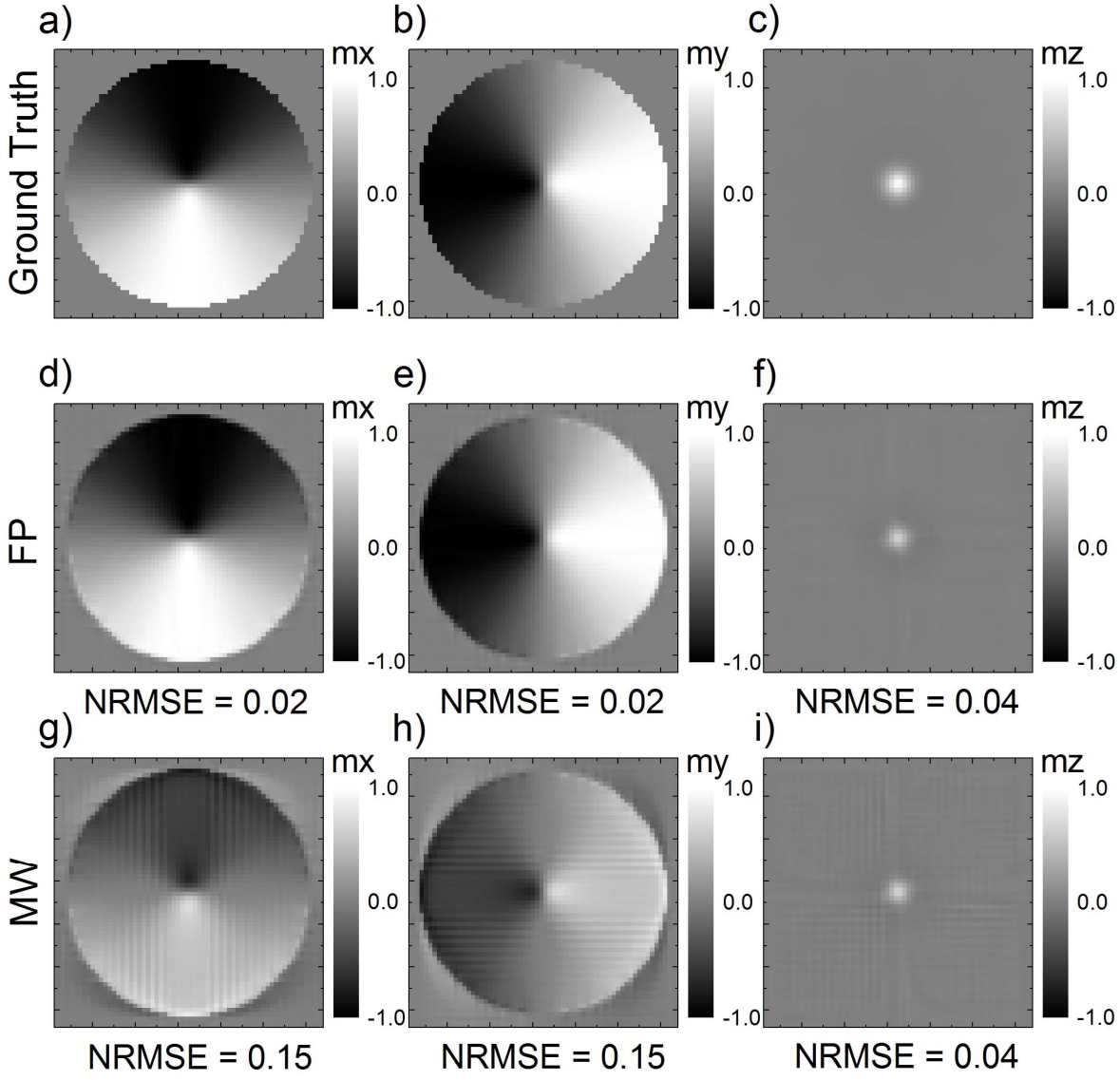

Figure 3 Ground truth [mx (a), my (b), mz (c)], full projection [mx (d), my (e), mz (f)] and missing wedge [mx (g), my (h), mz (i)] reconstructions of the disc particle. Images correspond to Z layer 32 of the volume model. Normalized root mean square error is indicated for the specific images.

In order to completely validate the reconstruction method, we investigate tomograms with data from the full projection (FP) range (-90 to 90 degrees, 1 degree step), and tilt series with a limited number of projections (Missing Wedge, MW). We have chosen for the latter a range from -60 to 60 degrees with 1 degree step. This limitation is typical of X-ray transmission tomography set-ups [18, 20]. The nano-disc and micro-square particles have been reconstructed taking 64 and 46 Z layers in the volume model respectively. Figure 3 presents the comparison between ground truth and the reconstructed data for the nano-disc particle in the 32nd Z layer of the volume. Components X, Y and Z of the

reconstructed vector field are shown for the FP and MW situations. Moreover, in order to quantify the quality of the reconstructions, the Normalized Root Mean Square Error (NRMSE) of the reconstruction compared with the ground truth is presented. This parameter is calculated as follows:

$$NRMSE = \frac{1}{X_{\max} - X_{\min}} \sqrt{\frac{1}{N}\sum_{i=1}^{N}\left(X_{GT} - X\right)^2} \quad (11)$$

X represents the data contained in the reconstructed model slice to be analysed; X_{GT} is the ground truth data; X_{min} and X_{max} are the minimum and maximum values of the pixels in the analysed slice respectively; and N is the total number of pixels involved. The high quality of the reconstructions is directly observed for MW and FP situations. However, the latter presents an excellent agreement with the ground truth data, while the value of all vector components in the MW case is smaller than the original one (5 – 20%).

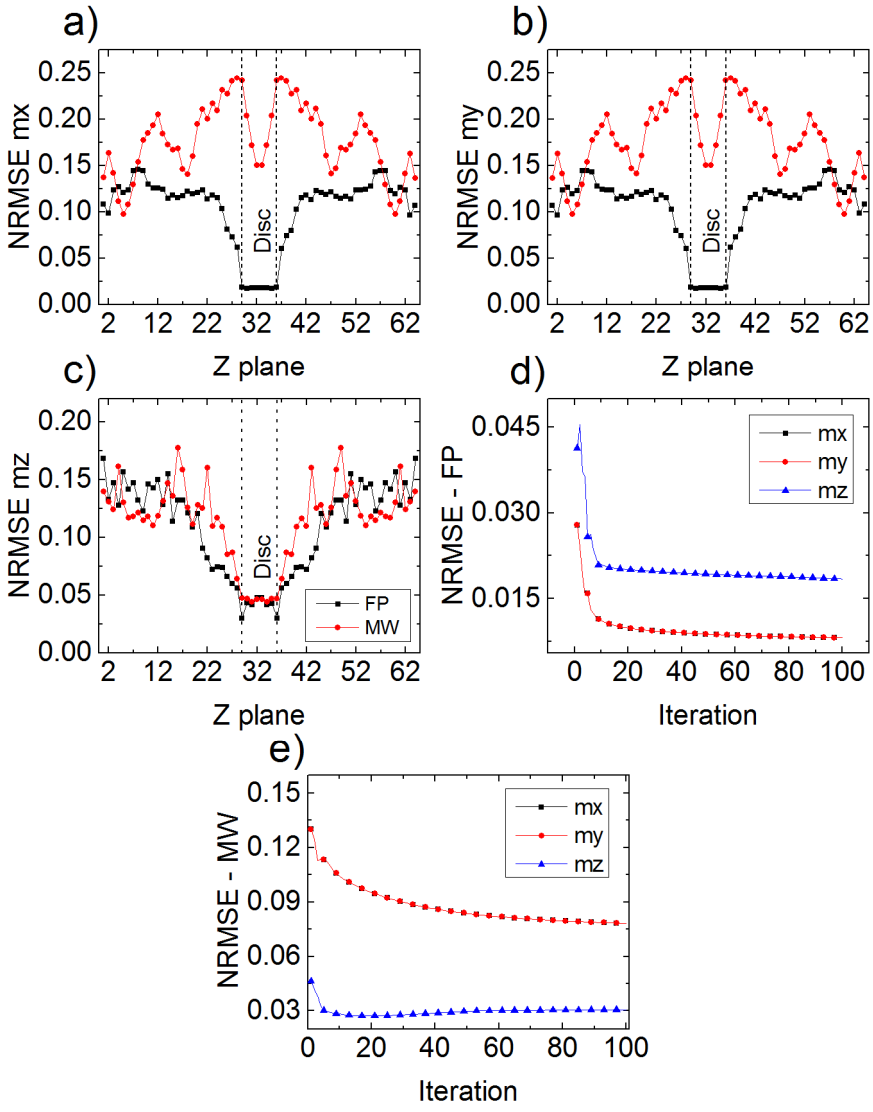

Figure 4 Normalized root mean square error from the reconstructed m_x (a), m_y (b) and m_z (c) of the nano-disc as a function of the Z layer. Full projection (FP, black squares) and missing wedge (MW,

red dots) situations are analysed. Dashed vertical lines indicate where the disc is located. NRMSE for the whole volume model as function of iterations in the FP (d) and MW (e) situations. Components mx (black squares) and my (red dots) present almost the same behaviour and appear superimposed.

We have analysed also the NRMSE for all the Z slices of the reconstruction volume to observe the MW effects along the thickness in the reconstructed solution (Fig. 4). Vertical dashed lines have been superimposed in the graphs where the edges of the disc are present. The results for the estimated error of X [Fig. 4(a)] and Y [Fig. 4(b)] components are almost equal, while the Z [Fig. 4(a)] one presents a different behaviour. This occurs because the information for the reconstruction of the Z component is present in *Xtilt* and *Ytilt* series, while the others components are reconstructed from the information of individual series. The evolution of the NRMSE calculated for the whole reconstructed volume model instead of by Z layer is presented for FP [Fig. 3(d)] and MW [Fig. 3(e)] situations. The MW case presents in general larger error than the full projection one. The reconstruction of the nanodisc top and bottom surfaces is also affected by the MW configuration leading to an ambiguity at the borders. It is important to mention here that the increased error associated to the MW series is manly associated to X and Y components. The out-of-plane component presents almost the same error in FP (NRMSE = 0.02) and MW (NRMSE = 0.03) situations; the only difference here is a small oscillation in the NRMSE vs iterations. In any case, both reconstructions clearly allow identifying the disc structure at the centre of the model volume and its magnetic configuration.

In the case of the magnetic micro-square heterostructure, the direct comparison between ground truth and reconstructions is presented in figures 5 and 6. The first one shows the 16^{th} Z slice (thick Py region), while the second represents the 38^{th} Z slice (thin Py region).

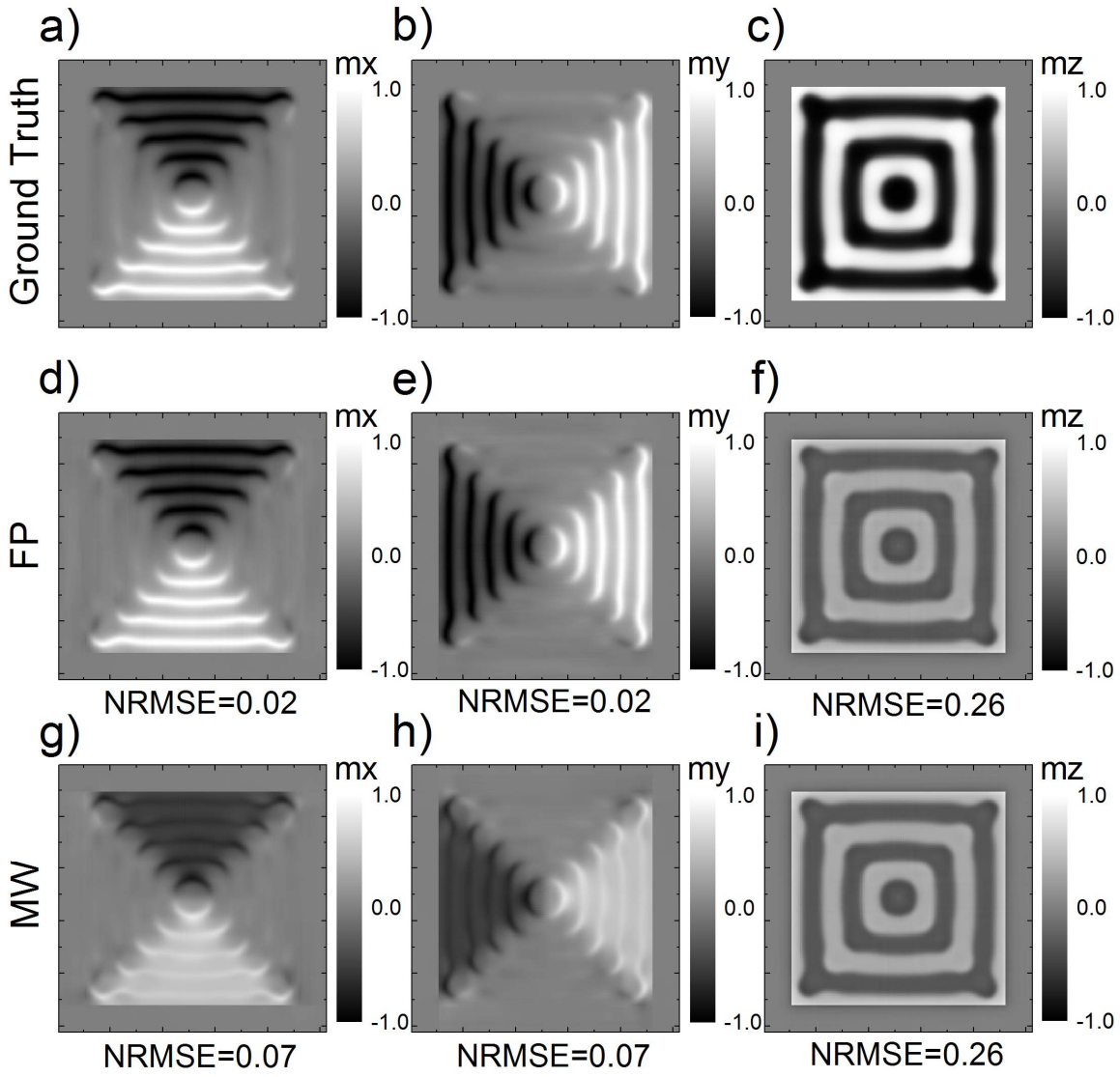

Figure 5 Ground truth [mx (a), my (b), mz (c)], full projection [mx (d), my (e), mz (f)] and missing wedge [mx (g), my (h), mz (i)] reconstructions of the square particle. Images correspond to Z layer 16 of the volume model. NRMSE is indicated for the specific images.

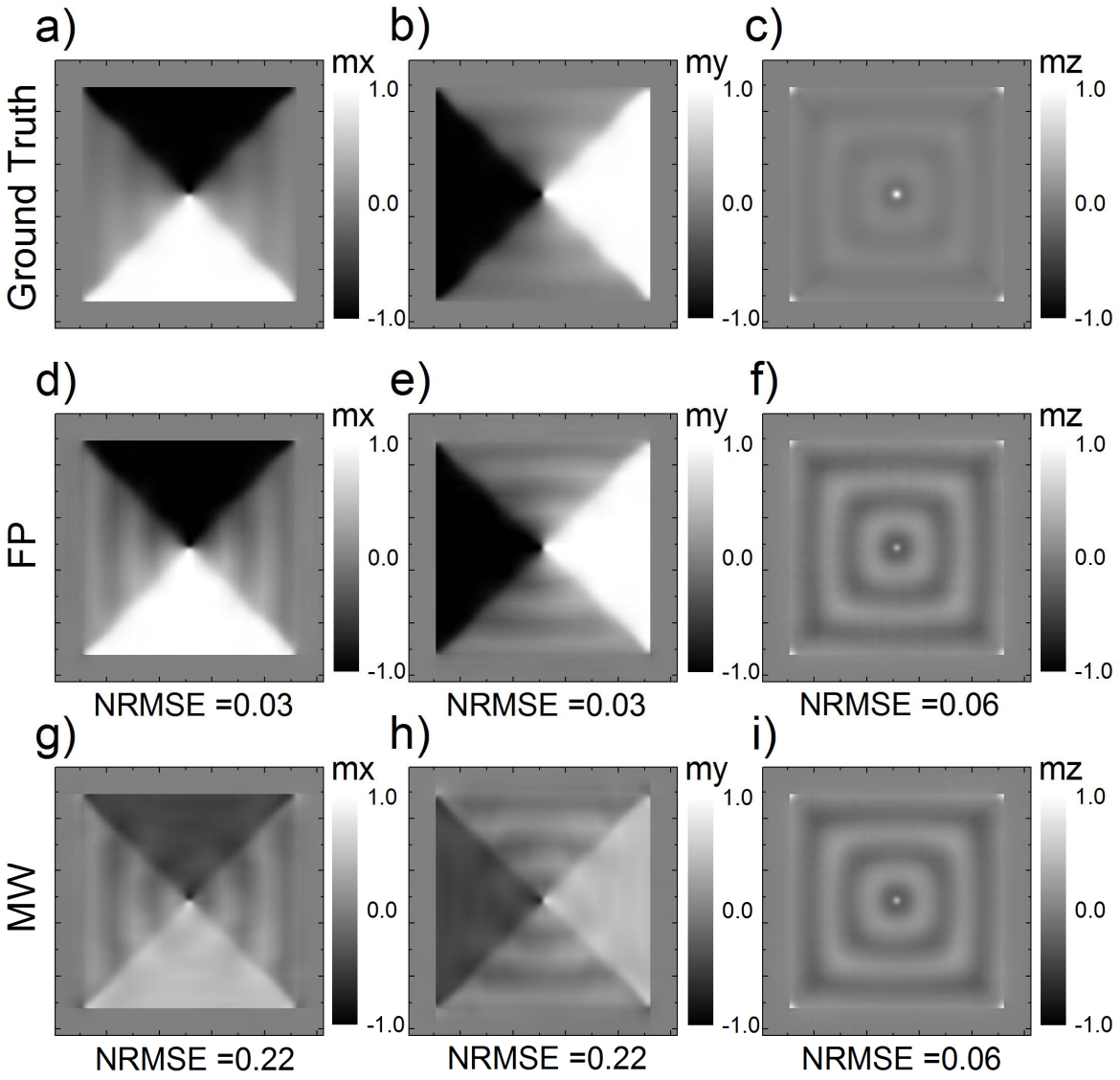

Figure 6 Ground truth [mx (a), my (b), mz (c)], full projection [mx (d), my (e), mz (f)] and missing wedge [mx (g), my (h), mz (i)] reconstructions of the square particle. Images correspond to Z layer 38 of the volume model. NRMSE is indicated for the specific images.

Again, FP and MW situations are studied. The latter presents a smaller intensity in all the reconstructed components and the agreement of the FP range reconstruction is much better than the MW one. It is important to mention here that the NRMSE for the Z component of the vector presents almost the same value for MW and FP reconstructions in the out-of-plane dominated area of the magnetic structure.

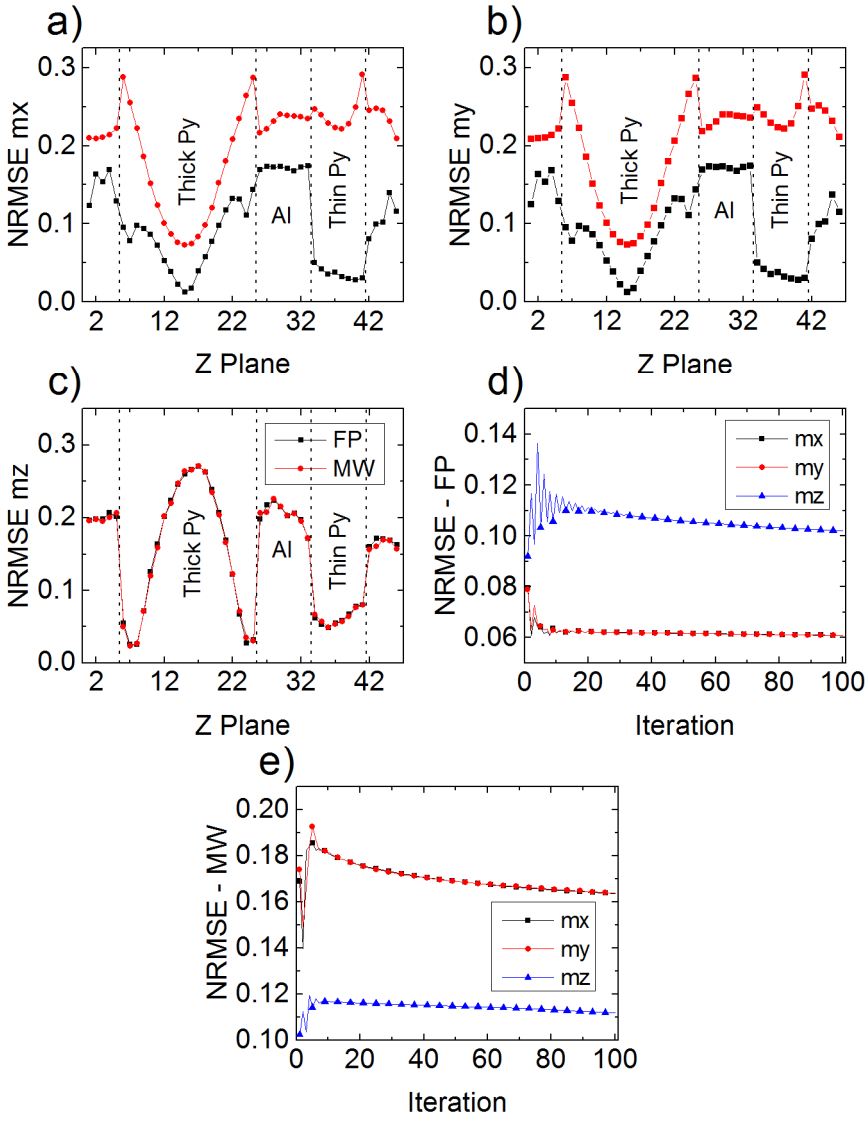

Figure 7 Normalized root mean square error from the reconstructed mx (a), my (b) and mz (c) of the micro-square as a function of the Z layer. Full projection (FP, black squares) and missing wedge (MW, red dots) situations are analysed. Dashed vertical lines indicate where different materials are located. NRMSE for the whole volume model as function of iterations in the FP (d) and MW (e) situations. Components mx (black squares) and my (red dots) present almost the same behaviour and appear superimposed.

The aforementioned effect in the error is clearly observed in the NRMSE representation as a function of the Z slice of the volume model for all the vector components (Fig. 7). The Z component presents a maximum in the error for the region where the out-of-plane magnetization dominates (thick Py region), and in the range dominated by m_x and m_y, the NRMSE decreases. This implies that it is harder to reconstruct the Z component despite the redundancy in the tomographic data (Z component reconstructed from both tilt series). This can be also observed in the convergence plots showing the NRMSE calculated for the whole reconstructed model as a function of the iteration number [Fig. 7(d)

and (e)]. Again, the main difference between MW and FP is an important increase in the error associated to the in-plane components while the value for the Z component is almost the same. It is also observed that the MW induces artifacts at the interfaces inside the object between different layers of the heterostructure. These artifacts are due to the missing data and conventional tomography also experiences such artefacts, especially for in situ imaging studies where the sample is in a chamber or cell and not all views are accessible with X-rays. However, the trend of the reconstructed vector field is qualitatively and in some cases quantitatively in agreement with the original magnetization configuration, indicating that the algorithm is capable of successfully reconstructing the 3D magnetization from Magnetic Soft X-ray Transmission Tomograms.

5. Conclusions

A new method to reconstruct the magnetization vector field of arbitrary magnetic systems using Soft X-ray Transmission Tomography has been described. The method takes advantage of the natural high dichroic contrast of magnetic materials at soft X-ray energies which leads in practice to acquisition times of only a few hours to achieve expected resolutions around 40 nm or better. The technique is useful to characterize magnetic samples with thicknesses up to ~300 nm and up to several μm of lateral dimensions. Both, scalar and vector reconstruction problems have been analysed in detail and solved by using ART. The vector case requires two differently oriented tilt series to obtain the three components of the magnetization. To test the method, two different magnetic particles have been simulated, and their respective tomograms calculated. We have studied both, full projections and also incomplete series due to missing wedges to mimic actual experimental limitations. The results for the full projections are always better than for the missing wedge as expected; however, both approaches provide qualitative and even quantitative descriptions of the magnetic structures. The method is well suited for providing detailed information of the magnetization of buried magnetic structures or interfaces, and consequently appears to be a valid characterization technique of 3D magnetism in spintronic devices.

References

[1] Hubert, A. & Schaëfer R. (1998). *Magnetic Domains: The Analysis of Magnetic Microstructures*, Springer Berlin Heidelberg.
[2] Berger, A. & Pufall, M. R. (1999). *J. Appl. Phys.* **85**, 4583.
[3] Teixeira, J. M., Lusche, R., Ventura, J., Fermento, R., Carpinteiro, F., Araujo, J. P., Sousa, J. B., Cardoso, S. & Freitas, P. P. (2011). *Rev. Sci. Instrum.* **82**, 043209.
[4] Scheinfein, M. R., Unguris, J., Kelley, M. H., Pierce, D. T. & Cellota, R. J. (1990). *Rev. Sci. Instrum.* **61**, 2501.
[5] Unguris, J. (2001). *Magnetic Imaging and its Application to Materials,* edited by M. De Graef and Y. Zhu, Vol. 36, pp. 167–194, Academic Press, San Diego, CA.
[6] Locatelli, A. & Bauer, E. (2008). *J. Phys. Condens. Matter*, **20**, 093002.
[7] Foerster, M., Prat, J., Massana, V., Gonzalez, N., Fontsere, A., Molas, B., Matilla, O., Pellegrin, E. & Aballe, L. (2016). *Ultramicroscopy* **171**, 63–79.

[8] De Graef, M. (2001). *Magnetic Imaging and its Application to Materials*, edited by M. De Graef and Y. Zhu, Vol. 36, Chap. 2, Academic Press, San Diego, CA.
[9] McVitie, S., McGrouther, D., MacFadzean, S., MacLaren, D. A., O'Shea, J. J. & Benitez, M. J. (2015). *Ultramicroscopy* **152**, 57–62.
[10] Phatak, C., Beleggia, M. & De Graef, M. (2008), *Ultramicroscopy* **108**, 503–513.
[11] Prabhat, K. C., Mohan, K. A., Phatak, C., Bouman, C. & De Graef, M. (2017). *Ultramicroscopy* **182**, 131–144.
[12] Blanco-Roldán, C., Quirós, C., Sorrentino, A., Hierro-Rodriguez, A., Álvarez-Prado, L. M., Valcárcel, R., Duch, M., Torras, N., Esteve, J., Martín, J. I., Vélez, M., Alameda, J. M. & Ferrer, S. (2015). *Nat. Commun.* **6**, 8196.
[13] Fernandez-Pacheco, A., Streubel, R., Fruchart, O., Hertel, R., Fisher, P. & Cowburn, R. P. (2017). *Nat. Commun.* **8**, 15756.
[14] Donnelly, C., Guizar-Sicarios, M., Scagnolly, V., Gliga, S., Joller, M., Raabe, J. & Heyderman, L. J. (2017). *Nature* **574**, 328–331.
[15] Hierro-Rodriguez, A., Quirós, C., Sorrentino, A., Blanco-Roldán, C., Álvarez-Prado, L. M., Martín, J. I., Alameda, J. M., Pereiro, E., Vélez, M. & Ferrer, S. (2017). *Phys. Rev. B* **95**, 014430.
[16] Hierro-Rodriguez, A., Quirós, C., Sorrentino, A., Valcarcel, R., Estébanez, I., Álvarez-Prado, L. M., Martín, J. I., Alameda, J. M., Pereiro, E., Vélez, M. & Ferrer, S. (2017). *Appl. Phys. Lett.* **110**, 262402.
[17] Gürsoy, D., De Carlo, F., Xiao, X. & Jacobsen, C. (2014). *J. Synchrotron Rad.* **21**, 1188–1193.
[18] De Carlo, F., Gürsoy, D., Ching, D.J., Batenburg, J., Ludwing, W., Mancini, L., Marone, F., Mokso, R., Pelt, D., Sijbers, J., Rivers, M. (2018). *Meas. Sci. Technol.* **29**, no. 3.
[19] Pereiro, E., Nicolás, J., Ferrer, S. & Howells, M. R. (2009). *J. Synchrotron Rad.* **16**, 505–512.
[20] Olivares-Marín, M., Sorrentino, A., Rung-Chuan, L., Pereiro, E., Naeh-Lih, W. & Tonti, D. (2015). *Nano Lett.* **15**, 6932–6938.
[21] Sorrentino, A., Nicolás, J., Valcárcel, R., Chichón, F. J., Rosanes, M., Avila, J., Tkachuk, A., Irwin, J., Ferrer, S. & Pereiro, E. (2015). *J. Synchrotron Rad.* **22**, 1112–1117.
[22] Kak, A. C. & Slaney M. (1988). *Principles of Computerized Tomographic Imaging*, IEEE Press, New York.
[23] Siddon, R. L. (1988). *Med. Phys.* **12**, 252–255.
[24] Jacobs, F., Sundermann, E., De Sutter, B., Christiaens, M. & Lemahieu, I. (1998). *Journal of Computing and Information Technology - CIT* **6**, 89–94.
[25] Vansteenkiste, A., Leliaert, J., Dvornik, M., Helsen, M., Garcia-Sanchez, F. & Waeyenberge, B. V. (2014). *AIP Advances* **4**, 107133.
[26] Voltan, S., Cirillo, C., Snijders, H. J., Lahabi, K., Garcia-Santiago, A., Hernandez, J. M., Attanasio, C. & Aarts, J. (2016). *Phys. Rev. B* **94**, 094406.

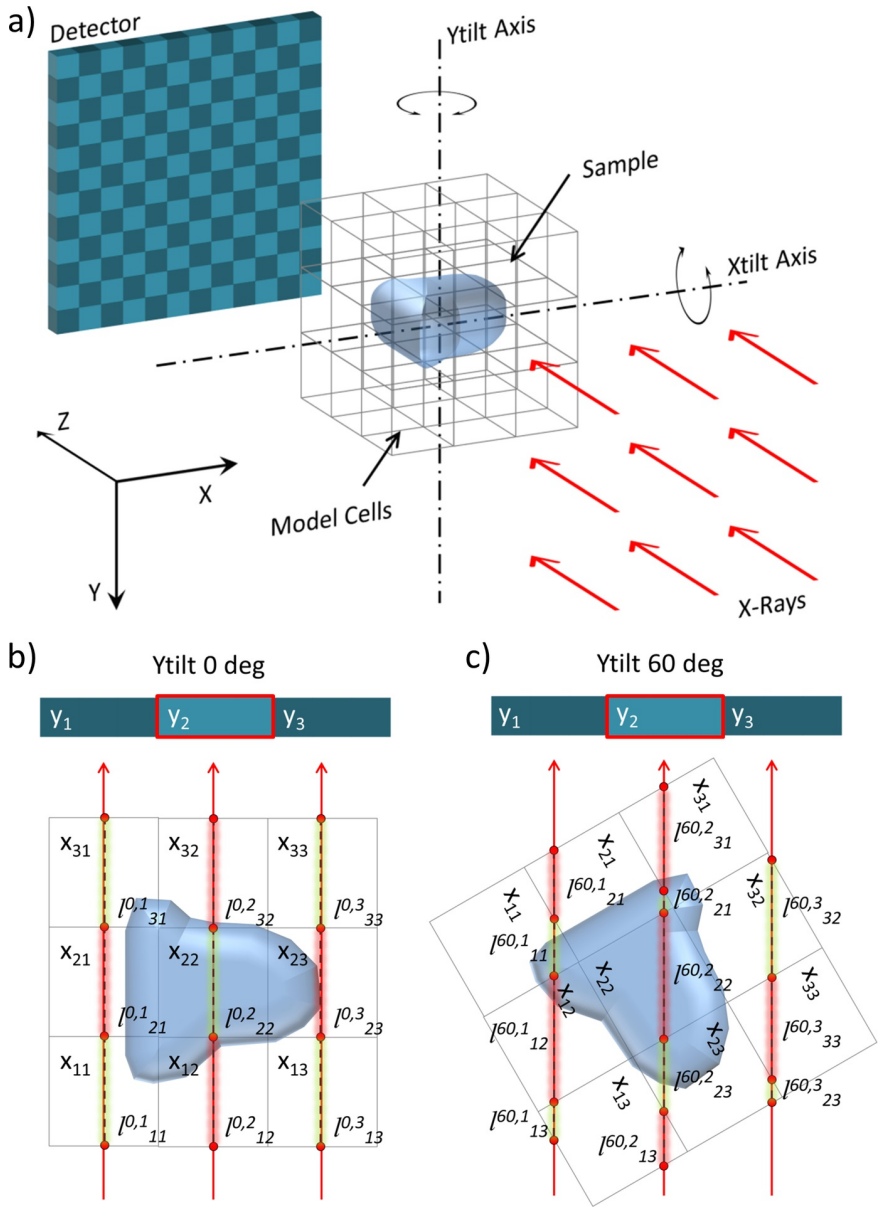
a)
Detector
Ytilt Axis
Sample
Xtilt Axis
Z
X
Y
Model Cells
X-Rays
b)
Ytilt 0 deg
y1
y2
y3
x31
x32
x33
x21
x22
x23
x11
x12
x13
c)
Ytilt 60 deg

Figure 1

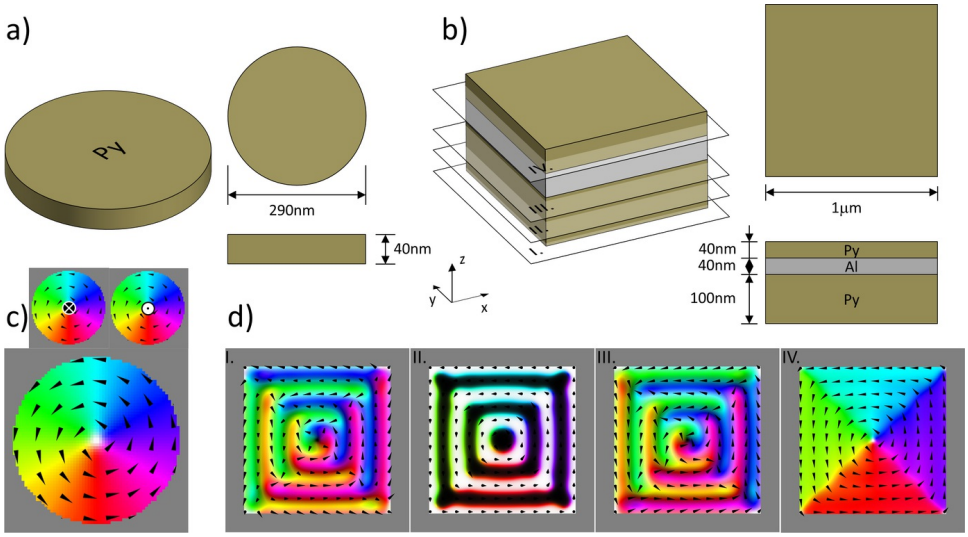

Figure 2

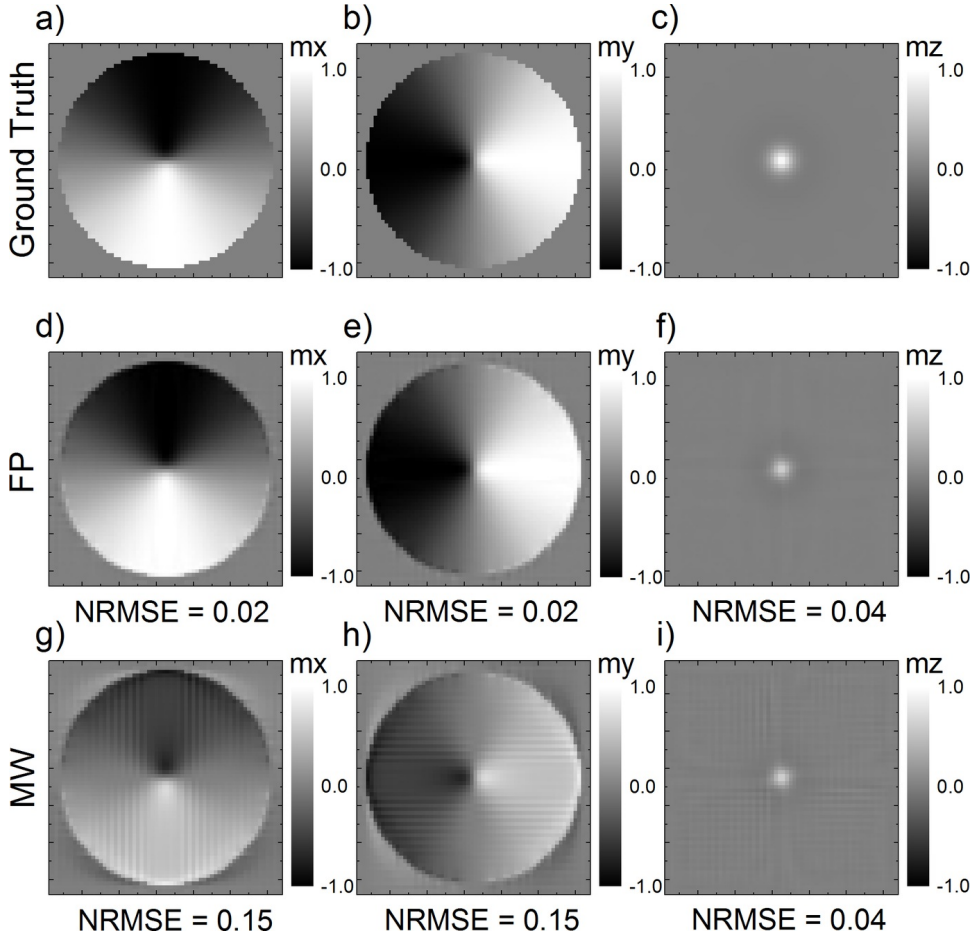
a)
b)
c)
Ground Truth
mx
my
mz
1.0
0.0
-1.0
d)
e)
f)
FP
NRMSE = 0.02
NRMSE = 0.02
NRMSE = 0.04
g)
h)
i)
MW
NRMSE = 0.15
NRMSE = 0.15
NRMSE = 0.04

Figure 3

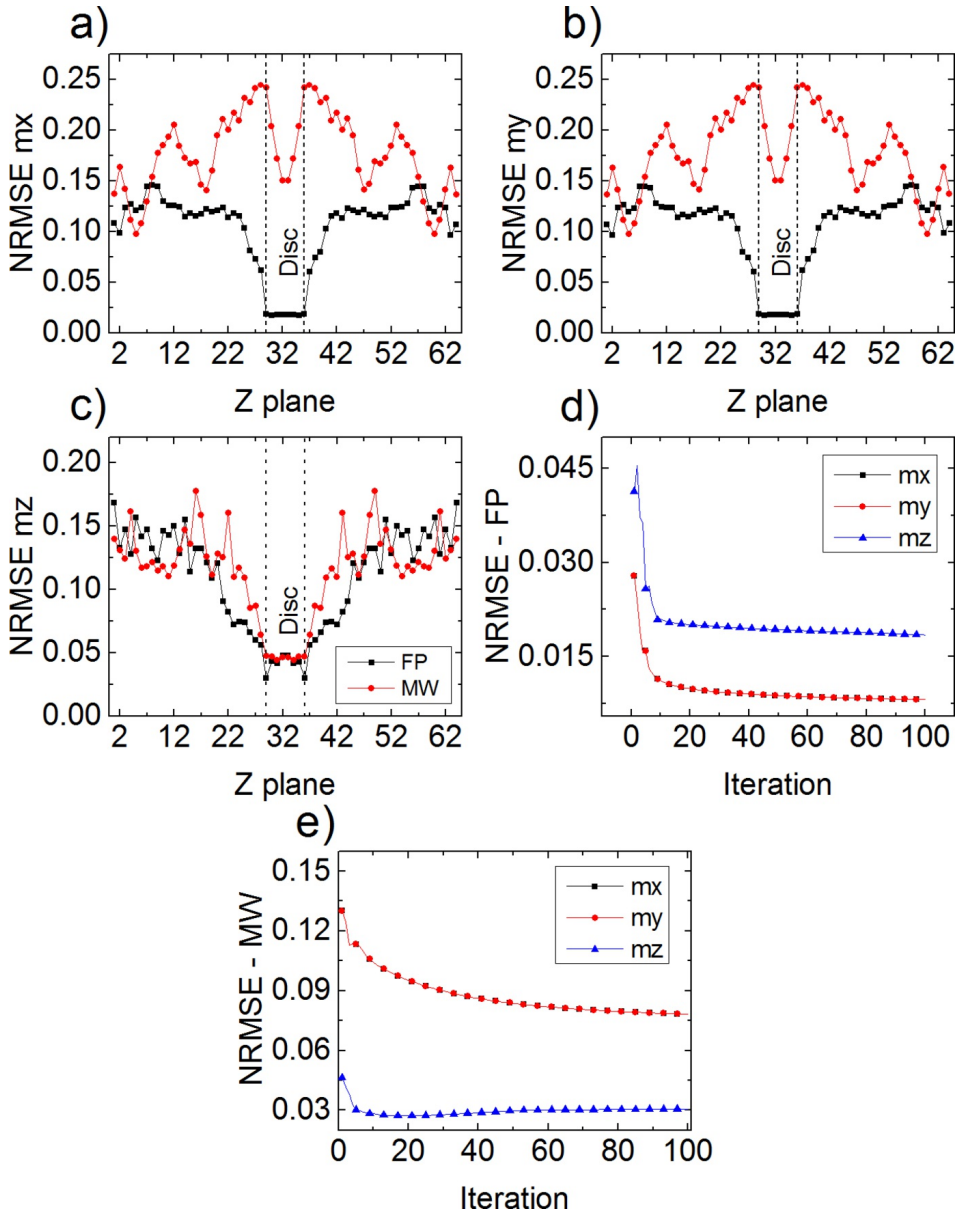
a)
NRMSE mx
Disc
Z plane
b)
NRMSE my
Disc
Z plane
c)
NRMSE mz
Disc
FP
MW
Z plane
d)
NRMSE - FP
mx
my
mz
Iteration
e)
NRMSE - MW
mx
my
mz
Iteration

Figure 4

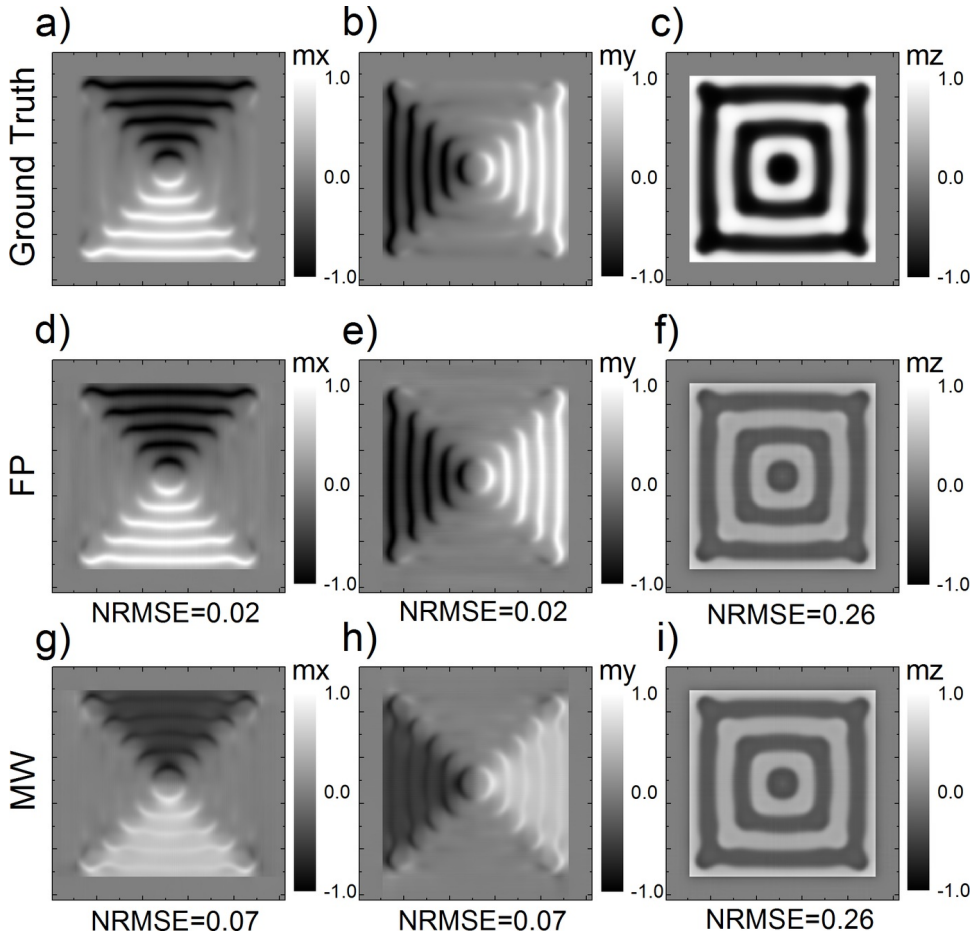
a)
b)
c)
Ground Truth
mx
my
mz
1.0
0.0
-1.0
d)
e)
f)
FP
NRMSE=0.02
NRMSE=0.02
NRMSE=0.26
g)
h)
i)
MW
NRMSE=0.07
NRMSE=0.07
NRMSE=0.26

Figure 5

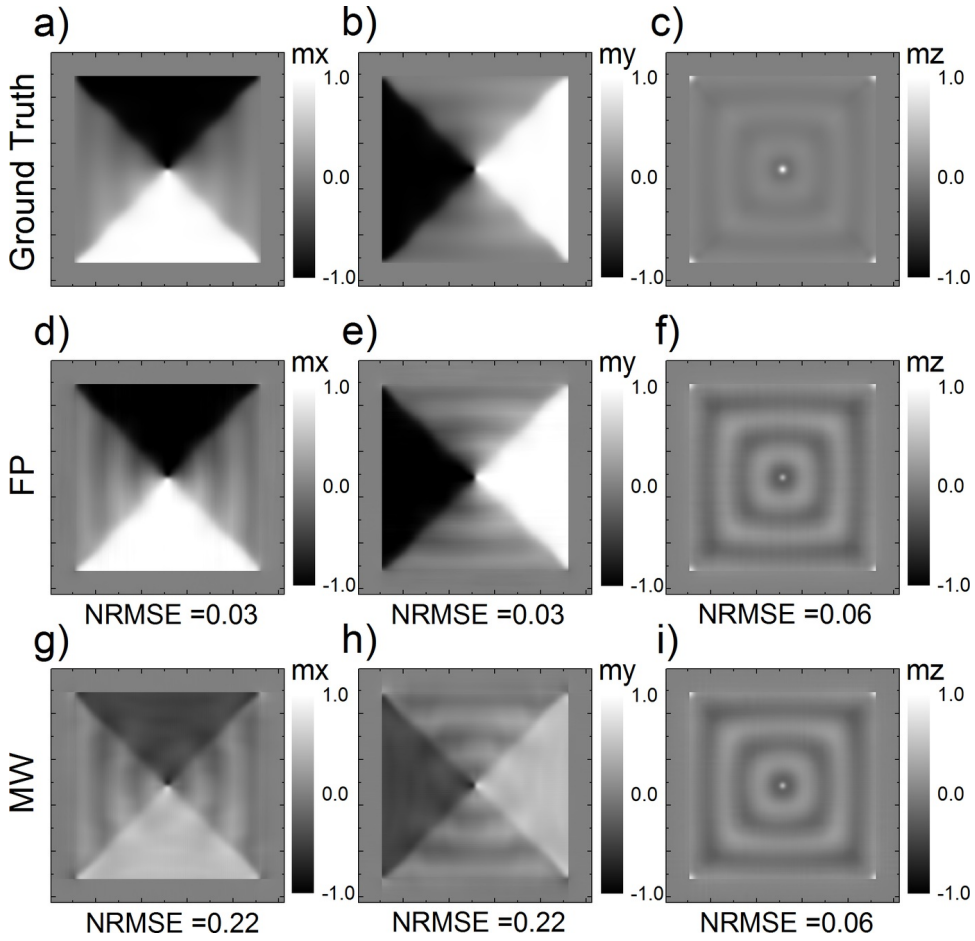
a)
b)
c)
Ground Truth
mx
my
mz
1.0
0.0
-1.0
d)
e)
f)
FP
NRMSE =0.03
NRMSE =0.03
NRMSE =0.06
g)
h)
i)
MW
NRMSE =0.22
NRMSE =0.22
NRMSE =0.06

Figure 6

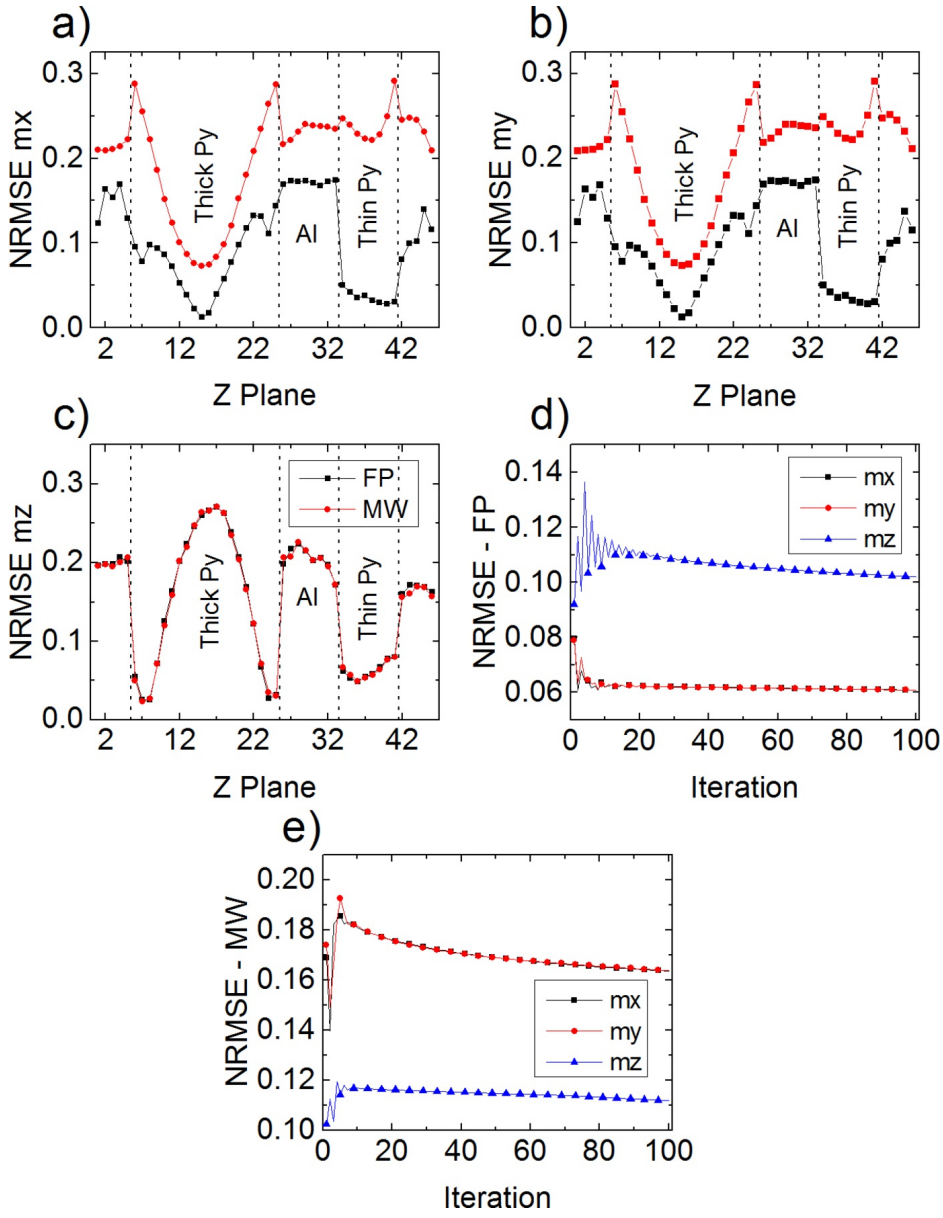
a)
NRMSE mx
Thick Py
Al
Thin Py
Z Plane
b)
NRMSE my
Thick Py
Al
Thin Py
Z Plane
c)
NRMSE mz
FP
MW
Thick Py
Al
Thin Py
Z Plane
d)
NRMSE - FP
mx
my
mz
Iteration
e)
NRMSE - MW
mx
my
mz
Iteration

Figure 7